

2D Relativistic MHD Simulations of the Kruskal-Schwarzschild Instability in a Relativistic Striped Wind

Ramandeep Gill,^{1,2}[★] Jonathan Granot,¹[†] and Yuri Lyubarsky²[‡]

¹Department of Natural Sciences, The Open University of Israel, 1 University Road, PO Box 808, Raanana 4353701, Israel

²Physics Department, Ben-Gurion University, P.O.B. 653, Beer-Sheva 84105, Israel

Last updated; in original form

ABSTRACT

We study the linear and non-linear development of the Kruskal-Schwarzschild Instability in a relativistically expanding striped wind. This instability is the generalization of Rayleigh-Taylor instability in the presence of a magnetic field. It has been suggested to produce a self-sustained acceleration mechanism in strongly magnetized outflows found in active galactic nuclei, gamma-ray bursts, and micro-quasars. The instability leads to magnetic reconnection, but in contrast with steady-state Sweet-Parker reconnection, the dissipation rate is not limited by the current layer's small aspect ratio. We performed two-dimensional (2D) relativistic magneto-hydrodynamic (RMHD) simulations featuring two cold and highly magnetized ($1 \leq \sigma \leq 10^3$) plasma layers with an anti-parallel magnetic field separated by a thin layer of relativistically hot plasma with a local effective gravity induced by the outflow's acceleration. Our simulations show how the heavier relativistically hot plasma in the reconnecting layer drips out and allows oppositely oriented magnetic field lines to reconnect. The instability's growth rate in the linear regime matches the predictions of linear stability analysis. We find turbulence rather than an ordered bulk flow near the reconnection region, with turbulent velocities up to $\sim 0.1c$, largely independent of model parameters. However, the magnetic energy dissipation rate is found to be much slower, corresponding to an effective ordered bulk velocity inflow into the reconnection region $v_{\text{in}} = \beta_{\text{in}}c$, of $10^{-3} \lesssim \beta_{\text{in}} \lesssim 5 \times 10^{-3}$. This occurs due to the slow evacuation of hot plasma from the current layer, largely because of the Kelvin-Helmholtz instability experienced by the dripping plasma. 3D RMHD simulations are needed to further investigate the non-linear regime.

Key words:

1 INTRODUCTION

Relativistic outflows are ubiquitous in the Universe. They are usually collimated into narrow jets, which are either observed directly, namely in active galactic nuclei (AGN; e.g. jets in M87 and Cygnus A), or inferred indirectly from multi-wavelength observations in X-ray binaries i.e. micro-quasars (e.g. Fender, Belloni, & Gallo 2004), gamma-ray bursts (GRBs; e.g. Kumar & Zhang 2015), and tidal disruption events (e.g. Krolik & Piran 2012). Relativistic outflows typically arise from accretion onto a rapidly spinning central compact object, such as a black hole (BH) or a neutron star (NS), which leads to the expulsion of matter and entrained magnetic fields at relativistic speeds. In pulsar winds and possibly in some GRBs the relativistic outflow is powered by the rotational energy of a rapidly rotating neutron star central source, rather than accretion. The launching, collimation, and acceleration of relativistic outflows

to high bulk Lorentz factors $\Gamma \gg 1$ in such a variety of systems is an active area of research.

The composition of relativistic jets or outflows in the different astrophysical sources, and in particular their degree of magnetization, is highly uncertain and of great interest. Pulsar winds are almost certainly Poynting flux dominated near the central source, and most likely so are the outflows from active galactic nuclei (AGN) and tidal disruption events (TDEs) of a star by a super-massive black hole. In AGN and TDEs, since the central accreting black hole is super-massive, then even close to it the Thomson optical depth τ_T may not be high enough for thermal acceleration by radiation pressure – the main competition to magnetic acceleration – to work efficiently (e.g. Ghisellini 2011). In GRBs or micro-quasars, however, thermal acceleration could also work ($\tau_T \gg 1$ is possible, or even likely), and the dominant acceleration mechanism is less clear. Nonetheless, there is a growing consensus that such outflows are launched hydro-magnetically with the magnetic fields playing a critical role (see for e.g. reviews by Spruit 2010; Pudritz, Hardcastle, & Gabuzda 2012; Granot et al. 2015).

Here we consider outflows that are at least initially Poynting

[★] Contact e-mail: rgill.rg@gmail.com

[†] Contact e-mail: granot@openu.ac.il

[‡] Contact e-mail: lyub@bgu.ac.il

flux dominated. One of the most important open questions about such outflows that start out highly magnetized near the central source is how they convert most of their initial electromagnetic energy to other forms, namely bulk kinetic energy and the energy in the random motions of the particles, which also produce the radiation we observe from these sources (i.e. the outflow acceleration, energy dissipation, particle acceleration and radiation). Observations of the relevant sources, such as AGN, GRBs or pulsar wind nebulae, suggest that the outflow magnetization σ (the Poynting-to-matter energy flux ratio) is rather low at large distances from the source. This is known as the σ problem, namely how to transform from $\sigma \gg 1$ near the source to $\sigma \ll 1$ very far from the source.

Poynting flux dominated outflows are often treated under the simplifying assumptions of ideal MHD, axi-symmetry and steady-state. However, under these conditions it is very hard to achieve $\sigma < 1$ (or $\sigma \ll 1$) far from the source that would enable efficient energy dissipation in internal shocks (Komissarov et al. 2009; Lyubarsky 2009, 2010a; Tchekhovskoy et al. 2008, 2009, 2010), where the acceleration requires external pressure confinement and is tightly coupled to the collimation of the jet. While this process could lead to $\sigma \approx 1$ this requires rather restrictive conditions.

Alternatively, the non-axi-symmetric kink instability could randomize the direction of the magnetic field, causing it to behave more like a fluid and enhancing magnetic reconnection, which both increase the acceleration and help lower the magnetization (Lyubarsky 1992; Eichler 1993; Spruit et al. 1997; Begelman 1998; Giannios & Spruit 2006; Bromberg & Tchekhovskoy 2016). However, such a global MHD instability could develop only if the proper Alfvén (lateral) crossing time is less than the propagation time, which implies $\Gamma\theta_{\text{jet}} < 1$, where Γ is the jet Lorentz factor and θ_{jet} is its half-opening angle. This condition is quite restrictive, e.g. it could hardly be fulfilled in GRBs (e.g. Tchekhovskoy et al. 2010). Moreover, even if the kink instability develops, it is still not clear whether the flow is disrupted or simply helically distorted.

An efficient conversion of electromagnetic energy into kinetic and thermal energy of the plasma is possible in impulsive flows that have a strong time variability (Granot, Komissarov & Spitkovsky 2011; Lyutikov 2011). The maximal Lorentz factor Γ and minimal magnetization σ that can be reached by a single thick shell (of a few tens of light seconds, comparable to the duration of a long GRB) is somewhat limited due to the interaction with the external medium (Levinson 2010; Granot 2012a). This may be alleviated if the outflow consists of many thinner, well separated sub-shells (Granot 2012a; Komissarov 2012), where even if the collisions between these sub-shells as they expand radially start at $\sigma \gg 1$ then gradual dissipation and subsequent acceleration can still occur via multiple passages of weak shocks.

An alternative option that we will focus on in this work involves magnetic energy dissipation in a striped wind. The prime example of a striped wind is a pulsar wind, where the pulsar acts as an oblique rotator with misaligned rotation and magnetic field symmetry axes, where the magnetic field of the outflowing MHD wind in the equatorial belt switches its polarity twice in each rotation period. The structure of the magnetic field advected at velocity v with the particle outflow is that of a *striped*-wind (Michel 1971; Coroniti 1990; Michel 1994; Lyubarsky & Kirk 2001), with field lines reversing polarity over a lab-frame length scale of $\lambda_B \approx \pi v/\Omega$. The polarity reversal between columns of magnetic field is marked by the presence of a current sheet towards which the magnetized fluid flows at a fraction of the Alfvén speed in the fluid-frame. Magnetic reconnection in these current layers helps accelerate the flow

and heats up particles creating a relativistically hot plasma in these current layers.

In pulsar winds a striped-wind arises naturally and magnetic field dissipation has been shown to be the main energy conversion mechanism there (Lyubarsky & Kirk 2001; Kirk & Skjæraasen 2003; Pétri & Lyubarsky 2007; Sironi & Spitkovsky 2011). Moreover, a broadly similar magnetic field configuration in the outflow may arise from accretion onto a black hole, due to stochastic flipping of the magnetic field polarity, possibly due to instabilities in the accretion disk (McKinney & Uzdensky 2012). This would result in a striped wind with shells of correspondingly random width and magnetic field polarity. Magnetic energy dissipation in a striped wind has received particular attention in the study of relativistic outflows ($\Gamma \gtrsim 100$) in GRBs, where the central engine (CE; a BH or a fast-rotating magnetar) launches a Poynting flux dominated outflow that suffers magnetic reconnection at a radial distance $r \sim 10^{12} - 10^{14}$ cm from the CE and produces the ~ 200 keV – MeV gamma-ray emission in the prompt-phase (e.g. Drenkhahn & Spruit 2002; Giannios 2008). In general, magnetic reconnection that does not necessarily result from having a striped-wind configuration has also been invoked in many works over the traditional internal-shock scenario to explain the prompt GRB emission due to it being more efficient in strongly magnetized flows (e.g. Thompson 1994; Lyutikov & Blandford 2003; Giannios & Spruit 2006; Lyutikov 2006; Zhang & Yan 2011).

Astrophysical plasmas near compact objects are inherently relativistic and collisionless (e.g. Lyutikov & Lazarian 2013), and they require some source of anomalous resistivity in order for reconnection to proceed. The rate of reconnection is set by the inflow velocity $v_{\text{in}} = \beta_{\text{in}}c$ of the magnetized fluid into the current layer. In fast reconnection models (e.g. Petschek 1964) it can be a fraction of the Alfvén speed, which approaches the speed of light in Poynting flux dominated outflows. It was shown by Lyubarsky (2005) and then confirmed using numerical simulations by e.g. Watanabe & Yokoyama (2006); Guo et al. (2015) that $\beta_{\text{in}} \sim 0.1$ when magnetic reconnection occurs in the relativistic Petschek regime.

It is worth noting that in most analytic and numerical works on reconnection the plasma is allowed to freely stream out of the region surrounding the X-point along the reconnection layer. In more realistic configuration featuring multiple X-points along the reconnection layer the hot plasma that is produced by the reconnection accumulates in the region between X-points and its dynamical effect can eventually slow down or even prevent further reconnection. This motivated search for mechanisms that could evacuate the hot plasma from the reconnection layer, which as a result would allow further reconnection and increase the reconnection rate.

This motivated the suggestion that magnetic reconnection in Poynting flux dominated relativistic outflows with a striped wind structure can be facilitated by the Kruskal-Schwarzschild instability (KSI) of the current sheet (Lyubarsky 2010b). This is an analog of the Rayleigh-Taylor instability (RTI) in strongly magnetized flows (e.g. Lyatsky & Goldstein 2013). It was shown that as the flow accelerates the current layer feels an effective (comoving) gravity $g = c^2 d\Gamma(r)/dr$ in the opposite direction. Since the enthalpy density of the relativistically hot plasma in the current layer is larger than that of the cold magnetized plasma below it, the current sheet becomes susceptible to the KSI just like an interface between a lighter fluid below a heavier one would be to the RTI. As the hot plasma drips out of the reconnection layer it allows further magnetic reconnection that produces more hot plasma and accelerates the flow, thus creating a positive feedback loop, and makes this instability self-sustained. Therefore, it can potentially account both

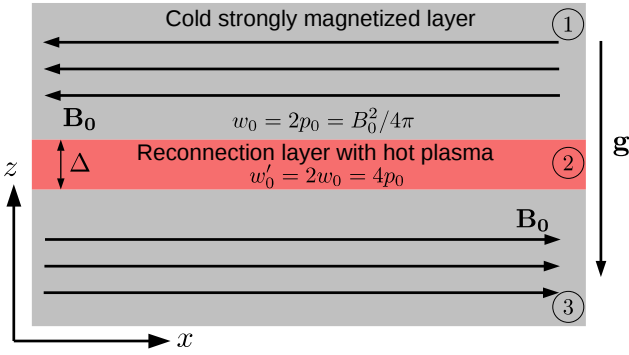


Figure 1. Striped wind with reconnecting layer in the comoving frame. The hot reconnection layer (2) of width Δ and enthalpy density w'_0 is surrounded by two (1 & 3) cold but strongly magnetized layers with magnetic field \mathbf{B}_0 . Here the field lines are shown as completely anti-parallel in the two layers, however, more generally they can also be slightly misaligned. The enthalpy density of the magnetized layers is $w_0 = w'_0/2$. As the flow accelerates in the \hat{z} direction, the layers feel an effective gravity $\mathbf{g} = -g\hat{z} = -c^2 d\Gamma(r)/dr\hat{z}$.

for the acceleration of the flow as well as for the energy dissipation, which leads to particle acceleration and the radiation that we observe. Moreover, this mechanism completely avoids the limitations of the classical Sweet-Parker resistive reconnection model and may yield fast reconnection rates. This is achieved by the downward (in the direction of the effective gravity force) dripping of hot plasma from the current layer where its removal is otherwise limited by the narrow width of the current layer in the Sweet-Parker model. By conservation of mass, faster removal of hot plasma from the current layer allows a faster inflow rate of cold magnetized gas, and thus a higher reconnection rate.

The focus of the present work is to quantitatively understand the structure and temporal evolution of the KSI using 2D relativistic MHD (RMHD) simulations. The primary goals are (i) to confirm the growth rate of the instability in the linear stage as calculated by Lyubarsky (2010b) using a linear stability analysis, and (ii) to obtain the energy dissipation rate in the non-linear regime, which can only be done using MHD simulations. To this end, in §2 we briefly discuss the results of the linear theory and in §3 present the numerical method used for the 2D simulations. We present the results from the simulations in §4, where we discuss perturbation modes with wavelength much larger and comparable to the width of the current layer. In §5, we infer the rate of reconnection from the rate of magnetic field dissipation in the simulated volume and discuss the role of the Kelvin-Helmholtz Instability (KHI) and buoyancy in limiting this rate in §6. We discuss some implications of this work in §7. We adopt Lorentz-Heaviside units and set the speed of light $c = 1$ throughout §3 - §6.

2 LINEAR STABILITY ANALYSIS

We consider a relativistically expanding outflow moving with bulk-Lorentz factor Γ . In the fluid-frame, we consider a non-magnetized, relativistically hot slab of plasma of width Δ , surrounded by a cold but strongly magnetized plasma with $\mathbf{B} = -\text{sign}(z)B_0\hat{x}$. The magnetic field has opposite polarity on either side of the current layer (see Fig. 1). The dynamical equations for the plasma, in the ideal MHD limit, follow directly from conservation laws (e.g. Landau &

Lifshitz 1966)

$$\partial_\mu(\rho u^\mu) = 0, \quad \partial_\mu T^{\mu\nu} = 0 \quad (1)$$

for $\mu = 0, 1, 2, 3$, where $\partial_\mu = (\partial/\partial(ct), \nabla)$ is the four-derivative, $u^\mu = (\gamma c, \gamma \mathbf{v})$ is the fluid four-velocity. The velocity \mathbf{v} and Lorentz factor $\gamma = [1 - (v/c)^2]^{-1/2}$ are measured in the outflow's bulk frame, in which the simulation is performed. The stress-energy tensor receives contributions from both the plasma and electromagnetic components, $T^{\mu\nu} = T_{\text{pl}}^{\mu\nu} + T_{\text{em}}^{\mu\nu}$, such that (e.g. Goedbloed, Keppens, & Poedts 2010)

$$T^{\mu\nu} = \frac{w u^\mu u^\nu}{c^2} + p \eta^{\mu\nu} - b^\mu b^\nu, \quad (2)$$

where $\sqrt{4\pi} b^\mu = [\gamma(\mathbf{B} \cdot \mathbf{v})/c, \mathbf{B}/\gamma + \gamma(\mathbf{B} \cdot \mathbf{v})\mathbf{v}/c^2]$ is the magnetic field four-vector, and $\eta^{\mu\nu} = \text{diag}(-1, 1, 1, 1)$ is the Minkowski metric. The enthalpy density in the fluid rest frame in each layer is

$$w = \rho c^2 + \frac{\hat{\gamma}}{\hat{\gamma} - 1} p \quad (3)$$

where ρ and p are the fluid-frame plasma mass density and pressure, and $\hat{\gamma}$ is the adiabatic index. In the strongly magnetized layer, the pressure is dominated by that of the magnetic field, for which $\hat{\gamma} \rightarrow 2$ and $p_B = B^2/8\pi$.

From Eq. (1), and keeping only the terms non-vanishing to first order in the perturbative expansion that follows, we find

$$\frac{\partial p}{\partial t} + \nabla \cdot (\rho \mathbf{v}) = 0, \quad (4)$$

$$w \frac{\partial \mathbf{v}}{\partial t} = -c^2 \nabla p + \frac{(\mathbf{B} \cdot \nabla) \mathbf{B}}{4\pi} + w \mathbf{g}. \quad (5)$$

The $(\mathbf{B} \cdot \nabla) \mathbf{B}/4\pi$ term represents the force due to magnetic tension, and $w \mathbf{g}$ is the effective gravity force felt by the fluid in the bulk-flow frame. As the flow accelerates in the \hat{z} -direction, the inertial acceleration is aligned in the opposite direction, $\mathbf{g} = -g\hat{z}$. These equations are further supplemented by the flux-freezing condition

$$\frac{\partial \mathbf{B}}{\partial t} = \nabla \times (\mathbf{v} \times \mathbf{B}), \quad (6)$$

and the equation of state

$$\frac{d}{dt} \left(\frac{p}{\rho^{\hat{\gamma}}} \right) = 0, \quad (7)$$

which expresses the adiabatic condition and only holds in the linear stage when no magnetic flux is destroyed by reconnection. The zeroth order equations, expressing the equilibrium state of the fluid, yield, $\partial \rho_0 / \partial t = \partial p_0 / \partial t = \partial w_0 / \partial t = \partial \mathbf{B}_0 / \partial t = 0$, and $\partial_x p_0 = \partial_y p_0 = 0$, with vertical pressure stratification condition due to the effective gravity

$$\partial_z p_0 = -\frac{w_0 g}{c^2}, \quad (8)$$

which for a homogeneous density has the solution

$$p_0(z) = p_0(0) - w_0 \frac{gz}{c^2} = p_0(0) \left[1 + \mathcal{O} \left(\frac{gz}{c^2} \right) \right], \quad (9)$$

suggesting that on length scales $z \ll c^2/g$, the pressure is also homogeneous. Furthermore, noting that in both the hot unmagnetized central layer and in the two cold but strongly magnetized layers $p_0 \sim w_0$, the pressure stratification condition leads to the result

$$\Delta \ll \frac{c^2}{g} \equiv L_{\text{dyn}}, \quad (10)$$

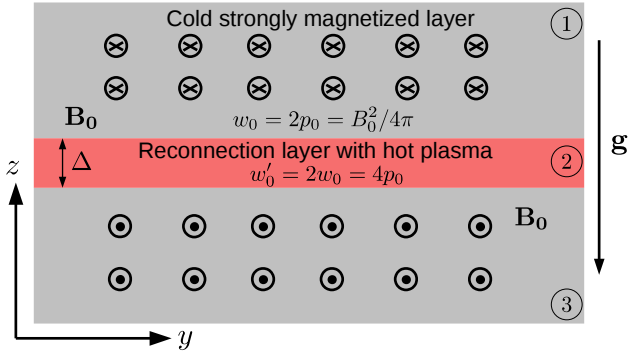


Figure 2. Setup of the simulation box, which is rotated here by 90° with respect to the illustration of the striped wind with a reconnecting layer as shown in Fig. 1. The magnetic field lines go into the page in region 1 and come out of the page in region 3.

in order to have a small fractional change in the initial pressure across the central layer. Here L_{dyn} is the dynamical length below which the effective gravity g is approximately constant and above which it may change significantly. This may be understood since $g = c^2 d\Gamma(r)/dr \sim c^2 \Gamma/r$ so that $c^2/g \sim r/\Gamma$ is of the order of the causal length in the radial direction. Defining the corresponding comoving dynamical time, $t_{\text{dyn}} \equiv L_{\text{dyn}}/c$, this corresponds to $gt_{\text{dyn}} \sim c$, i.e. a Newtonian free-fall velocity of order c is achieved over the dynamical time.

By considering small amplitude perturbations in the equilibrium quantities and adopting the ansatz that the perturbed quantities vary harmonically (e.g. $\rho_1 \propto \exp(i[ky - \omega t])$ where k is the wavenumber and ω is the wave frequency), Lyubarsky (2010b) (see for full derivation of the linear growth rate) obtained the following dispersion relation for modes orthogonal to the equilibrium magnetic field,

$$\omega_{\pm}^2 = \pm gk \left(5 + \frac{4}{\tanh(k\Delta)} \right)^{-1/2}. \quad (11)$$

The growth rate of the instability is then given by $\eta = \text{Im}(\omega_-)$, which asymptotes to the following in the small ($k\Delta \gg 1$) and large ($k\Delta \ll 1$) wavelength limits

$$\eta = \begin{cases} \sqrt{\frac{gk}{3}}, & k\Delta \gg 1 \\ \left(\frac{g}{2}\right)^{1/2} k^{3/4} \Delta^{1/4}, & k\Delta \ll 1. \end{cases} \quad (12)$$

3 2D NUMERICAL SIMULATIONS

To study the linear and non-linear growth rates and structure of the KSI, we have conducted MHD simulations in 2D using the publicly available code *Athena* (v4.2; Stone et al. 2008; Beckwith & Stone 2011). *Athena* is a grid-based code that can solve the equations of relativistic MHD (RMHD) using Godunov methods. The problem under study is inherently relativistic with adiabatic index $\hat{\gamma} = 4/3$ in the relativistically hot plasma layer, and therefore, we used the special relativity module of *Athena* with the HLLD Riemann solver, a third-order reconstruction of the primitive variables, and Van-Leer integrator.

The KSI is simulated in a box of size $(L_y, L_z) = (0.1, 0.2)$, where $-0.05 \leq y \leq 0.05$ and $-0.1 \leq z \leq 0.1$. The current layer

has (fluid-frame) width $\Delta = 0.01$ and the initial setup for the anti-aligned magnetic field case is shown in Fig. 2, where the strength of the equilibrium magnetic field is set by the magnetization σ of the cold plasma layer (here we set $c = 1$ and use Lorentz-Heaviside units so that factors of 4π are ignored; see Beckwith & Stone (2011) for equations of relativistic MHD in these units)

$$\sigma_0 \equiv \frac{w_{B,0}}{w_{m,0}} = \frac{b_0^2}{\rho_0 + 4p_g} \xrightarrow{\text{cold}} \frac{b_0^2}{\rho_0}, \quad (13)$$

where an adiabatic index of $\hat{\gamma} = 4/3$ has been assumed for a relativistically hot gas. The mass density in the cold magnetized layers is assumed to be $\rho_{0,c} = \rho_0 = 1$ with a density contrast $\rho_{0,h} = 3\rho_{0,c}$ in the hot unmagnetized layer. At the initial moment, all layers are assumed to be in pressure equilibrium with homogeneous pressure $p_0 = \sigma_0/2$. The characteristic velocity of the system is the relativistic Alfvén velocity

$$v_A = \sqrt{\frac{\sigma_0}{1 + \sigma_0}} = \sqrt{f_\sigma}, \quad (14)$$

where $0 \leq f_\sigma \equiv \sigma_0/(1 + \sigma_0) \leq 1$ is the fraction of the total energy in magnetic fields, and for which the crossing time $t_A = L_z/v_A$. Pressure homogeneity is maintained so long the condition given in Eq. (10) is met, with the magnitude of the effective gravity setting the scale of the simulation box $z \ll g^{-1}$. The code uses reflective boundary conditions in the \hat{z} -direction and periodic boundary conditions in the \hat{y} direction. To initiate the instability, the equilibrium state is perturbed by introducing a velocity perturbation of the form

$$v_{1z}(y, z) = \frac{v_1}{2} \left[\sin\left(\frac{2\pi m_0 y}{L_y}\right) \right] \left[1 + \cos\left(\frac{2\pi z}{L_z}\right) \right]. \quad (15)$$

where m_0 is the mode number in the \hat{y} -direction and the corresponding wavelength is $\lambda_0 = L_y/m_0$. This form of the perturbation ensures that no net momentum is imparted to the fluid elements in the simulation box. In addition, it is ensured that the perturbation velocity vanishes at the left and right boundary of the simulated region in order to suppress any spurious boundary effects. The perturbation amplitude is set to be a small fraction of the Alfvén speed, such that $\kappa_v \equiv v_1/v_A \ll 1$.

To measure the growth rate of the instability in the linear stage, we follow the treatment by Jun, Norman, & Stone (1995) and write the Fourier amplitude of the density perturbations as

$$f_m(z) = \frac{1}{L_y} \left| \int_{-L_y/2}^{L_y/2} \delta\rho(y, z) e^{-i2m\pi y/L_y} dy \right| \quad (16)$$

where the perturbations are obtained by using the measure $\delta\rho(y, z) = [\rho(y, z)/\bar{\rho}(z)] - 1$, which gives the amplitude of the density departure from the average density

$$\bar{\rho}(z) = \frac{1}{L_y} \int_{-L_y/2}^{L_y/2} \rho(y, z) dy. \quad (17)$$

The growth for a given mode m is then obtained by averaging the mode amplitude over different length scales $\Delta z = z_2 - z_1$ around the perturbed hot layer,

$$\langle f_m \rangle = \frac{1}{z_2 - z_1} \int_{z_1}^{z_2} f_m(z) dz. \quad (18)$$

In the following, temporal evolution of fluid quantities is shown using the simulation time. The time-step for the simulation depends on the resolution $\{N_y, N_z\} = \{512, 1024\}$ and the CFL number $\mathfrak{C} = 0.5$, such that $\Delta t = \mathfrak{C} \text{Min}[L_z/N_z, L_y/N_y] = 0.977 \times 10^{-4}$.

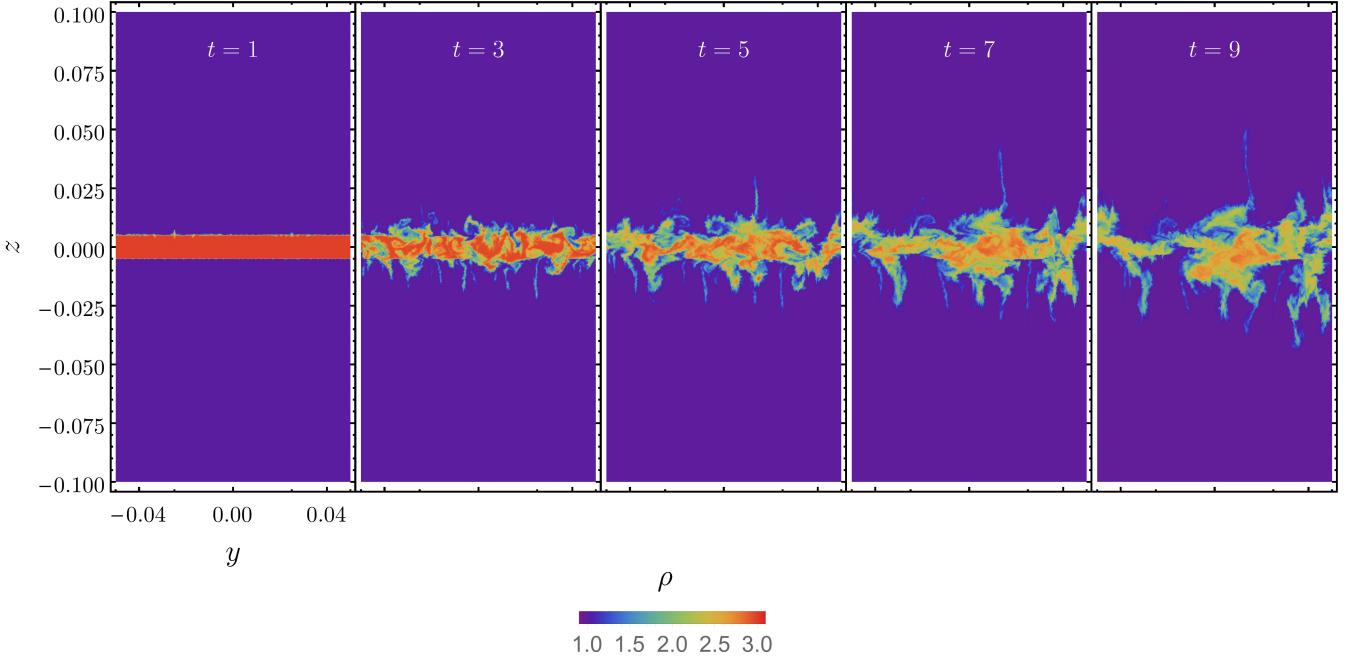


Figure 3. Development of the KSI from the linear to the non-linear stage, shown here using the fluid mass density, in the single wavelength ($m_0 = 1$) $\lambda_0 = 0.1$ case. The initial velocity perturbation amplitude $\kappa_v = v_1/v_A = 10^{-6}$ of the Alfvén speed in the magnetized layer. The effective gravity points downwards and has magnitude $g = 0.01$, which gives a causal size of $z = g^{-1} = 100$ over which pressure homogeneity is maintained. The magnetization $\sigma_0 = 10$ and the density contrast between the cold magnetized and the hot unmagnetized layer is $\rho_{0,h}/\rho_{0,c} \equiv \psi = 3$ with $\rho_{0,c} = 1$.

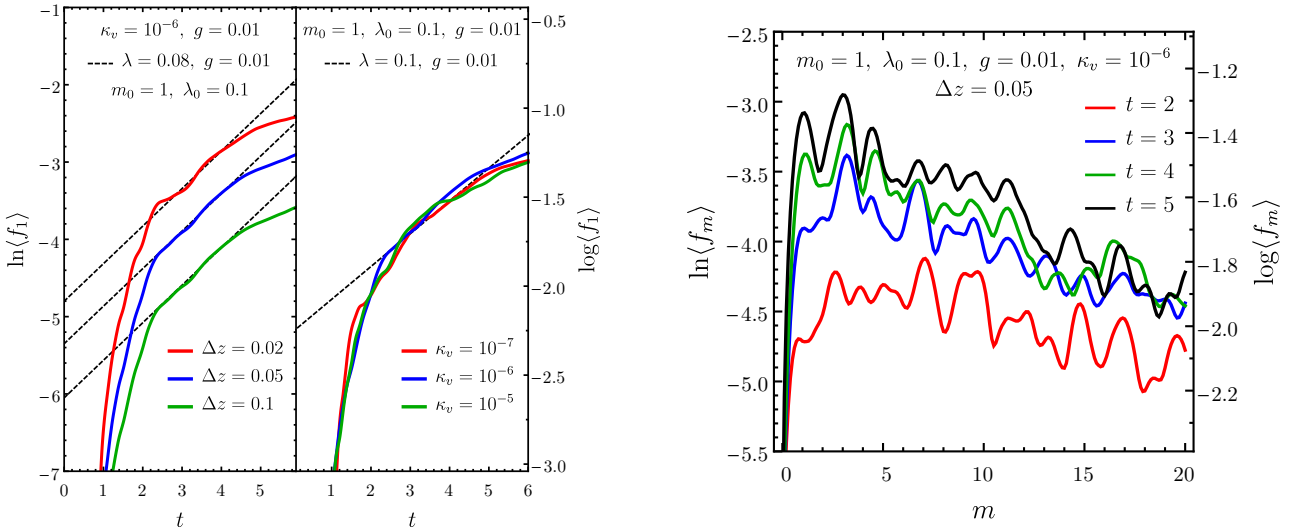


Figure 4. (Left) Growth of the density perturbation mode amplitude for the 2D simulation shown in Fig. 3. The spatially averaged Fourier mode amplitude for a given mode m grows exponentially with time in the linear regime, such that $\langle f_m \rangle \propto e^{\eta_m t}$, where η_m is the growth rate of the mode. Different curves show the growth rate of the single wavelength mode ($m = 1$) averaged in the \hat{z} -direction over different mixing regions of size Δz centered at the middle of the hot unmagnetized layer. Also shown is the dependence of $\langle f_1 \rangle$ on the magnitude of the initial velocity perturbation κ_v , while keeping $\Delta z = 0.05$. The prediction of the linear theory (with arbitrary normalization) from Eq.(11) for a mode with wavelength $\lambda \approx \lambda_0$ is shown with dashed lines. **(Right)** Temporal evolution of the mode spectrum.

4 SIMULATION RESULTS

In 2D the instability mode can either be transverse or parallel to the equilibrium magnetic field. Here we present results for the transverse case, which as expected evolves similarly to the hydrodynamic case since the magnetic field doesn't play any role in stabilizing the

instability. In the parallel case, unstable perturbations can be stabilized by magnetic field tension.

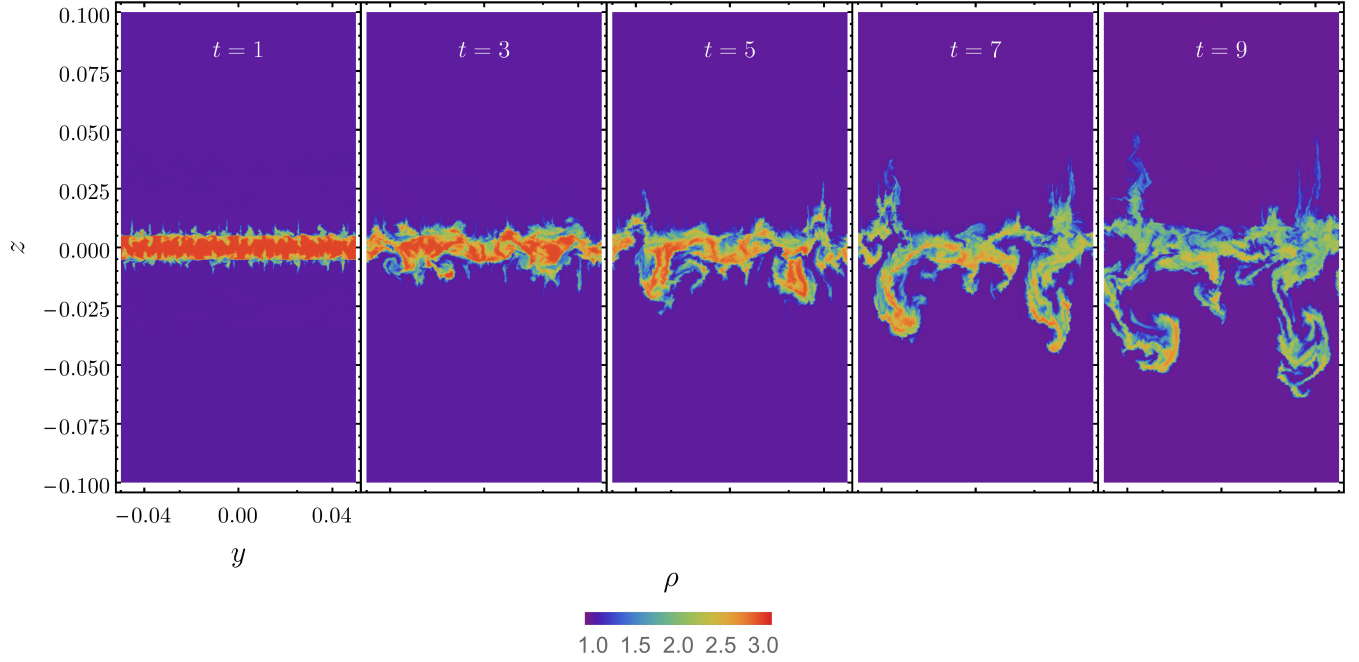


Figure 5. Development of the KSI for a higher value of $g = 0.1$, with the rest of the parameters same as Fig. 3.

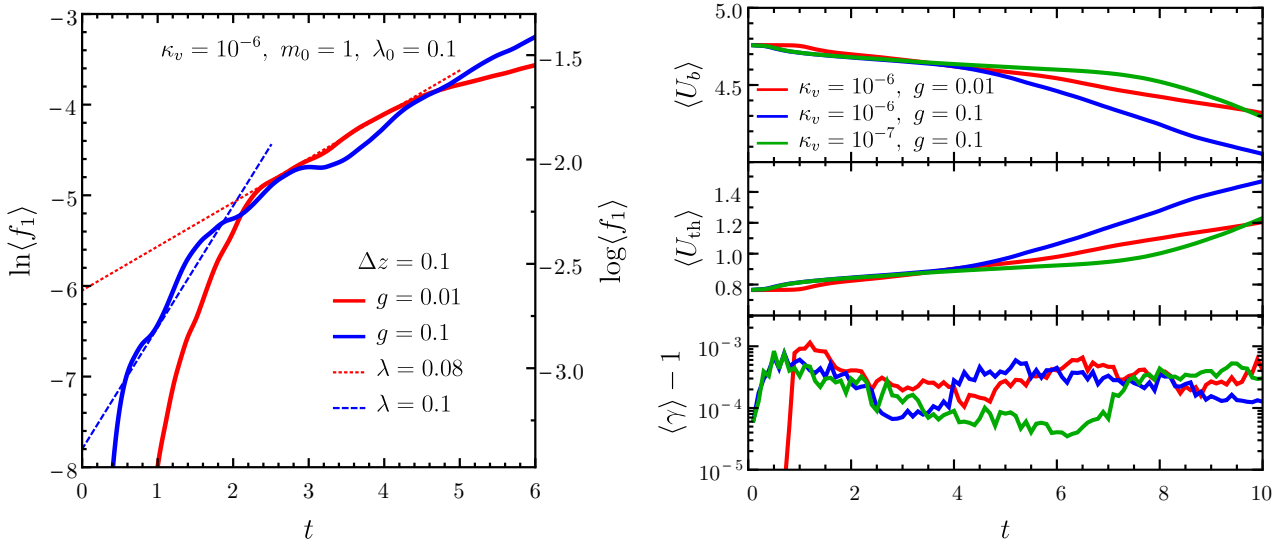


Figure 6. (Left) Comparison of growth rates obtained for the two cases with $m_0 = 1$ and $g = \{0.01, 0.1\}$ to that expected from linear theory (dashed & dotted lines; with arbitrary normalization). (Right) Temporal evolution of volume-averaged quantities for the single-wavelength ($m_0 = 1$) case shown in Fig. 3. Shown here are the magnetic field energy density (top), thermal energy density (middle), and the Lorentz factor of fluid elements (bottom) for two different velocity perturbation amplitudes and different effective gravity.

4.1 Large Wavelength ($k\Delta \ll 1$) Mode

It is instructive to first study the much simpler single wavelength mode, $m_0 = 1$, before undertaking more complicated scenarios. Fig. 3 demonstrates the development of the KSI for $m_0 = 1$ by showing snapshots of the plasma rest mass density ρ at different simulation times. The anti-aligned equilibrium magnetic field lines go into (out of) the page in the region above (below) the hot layer. The wavelength of the initial velocity perturbation is $\lambda_0 = L_y$ and we choose a small enough κ_v so that the instability is driven only

by the effective gravity and not by the initial conditions. To that end, we have carried out simulations to establish the upper limit on $\kappa_v < 10^{-5}$ below which the current layer remains stable for $g = 0$, such that the initial perturbations don't grow over time. On the other hand, a high $\kappa_v > 10^{-5}$ disrupts the hot layer, regardless of the magnitude of g , and drives the mixing of the two magnetized fluids, however, the instability in this case is artificial and not driven by the effective gravity.

The mode amplitude, averaged over the mixing region of extent

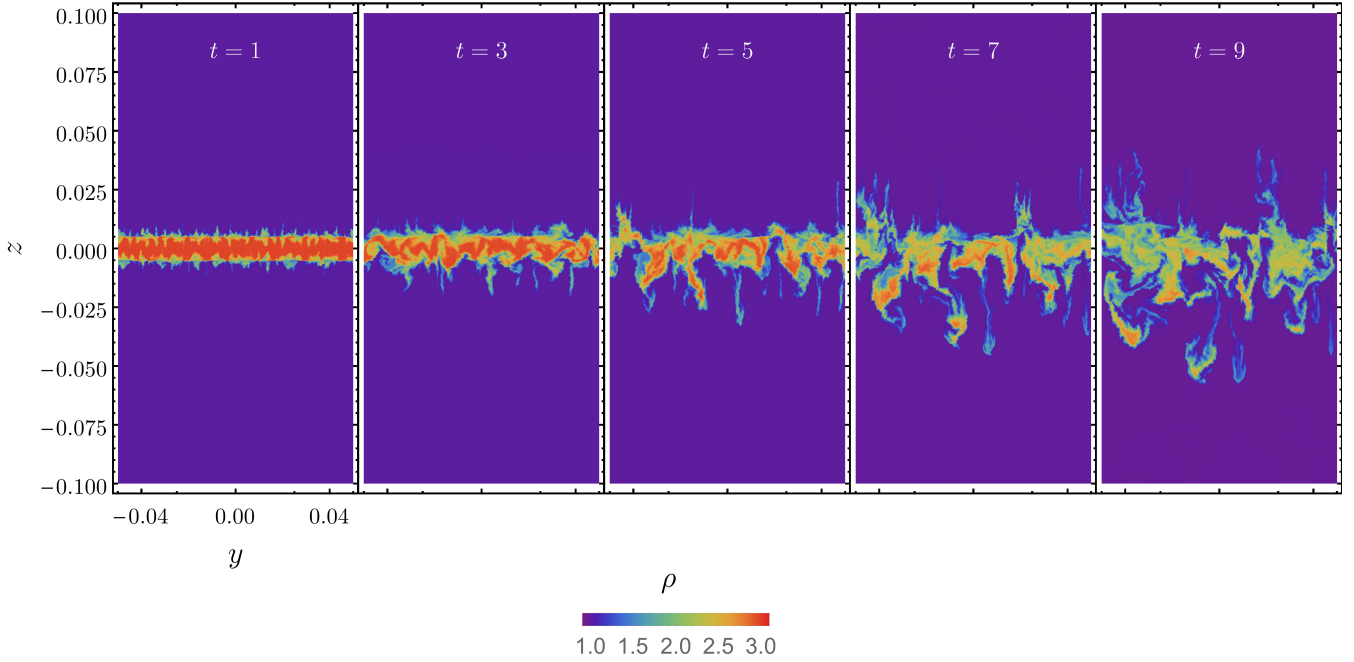


Figure 7. Development of the KSI from the linear to the non-linear stage for the high mode number ($m_0 = 10$) initial velocity perturbation case, with $\kappa_v = \nu_1/\nu_A = 10^{-7}$ and $g = 0.1$. The other parameters are the same as in Fig. 3.

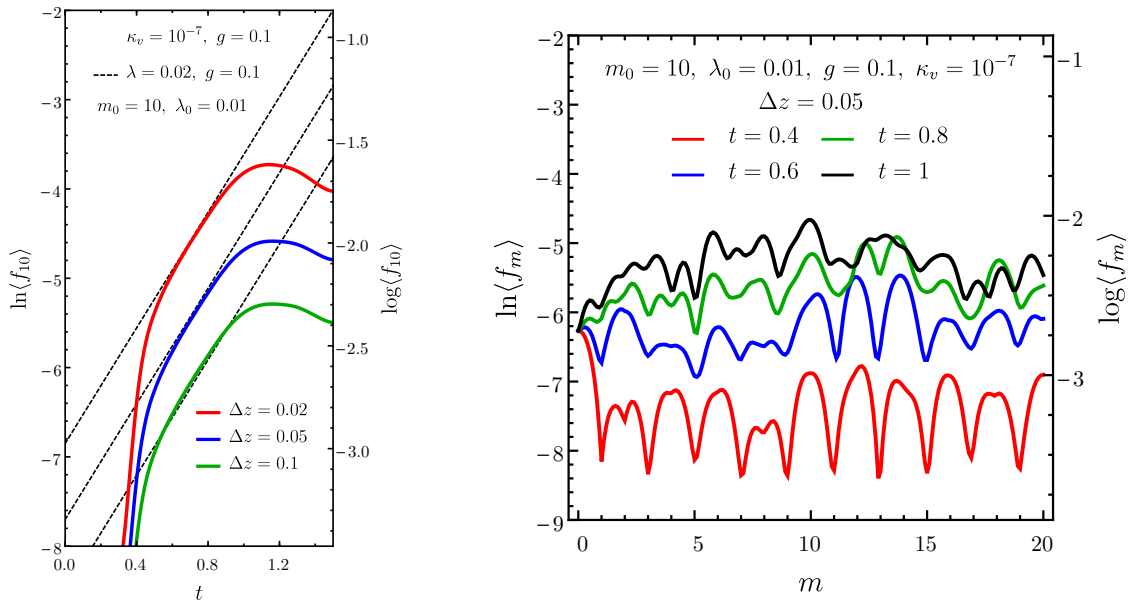


Figure 8. (Left) Growth of the density perturbation mode amplitude for the 2D simulation shown in Fig. 7. The three curves correspond to the Fourier amplitude of the mode $m = 10$ averaged over different mixing regions of size Δz centered at the middle of the hot unmagnetized layer. The prediction of the linear theory (with arbitrary normalization) from Eq. (11) for a mode with wavelength $\lambda \approx \lambda_0$ is shown with dashed lines. (Right) Temporal evolution of the mode spectrum in the linear stage for the simulation shown in Fig. 5.

Δz , should grow exponentially with time in the linear stage, such that $\ln\langle f_m \rangle \propto \eta_m t$. We plot this quantity for different sizes of the mixing region, Δz , in the left-panel of Fig. 4 and compare it with predictions from the linear theory, which are shown with arbitrary normalization since only their slope is relevant here. The different stages of the instability shares many similarities with the

RTI (compare with e.g. Fig. 6 of Jun, Norman, & Stone (1995)) and can therefore be understood in a similar manner.

The instability proceeds in three separate stages and its growth rate at any given time can be inferred from the slope of the curves in Fig. 4. (1) *Super-linear stage*: This stage simply reflects the response of the current layer to the initial condition where the interface is disturbed by the initial velocity perturbation. This excites several

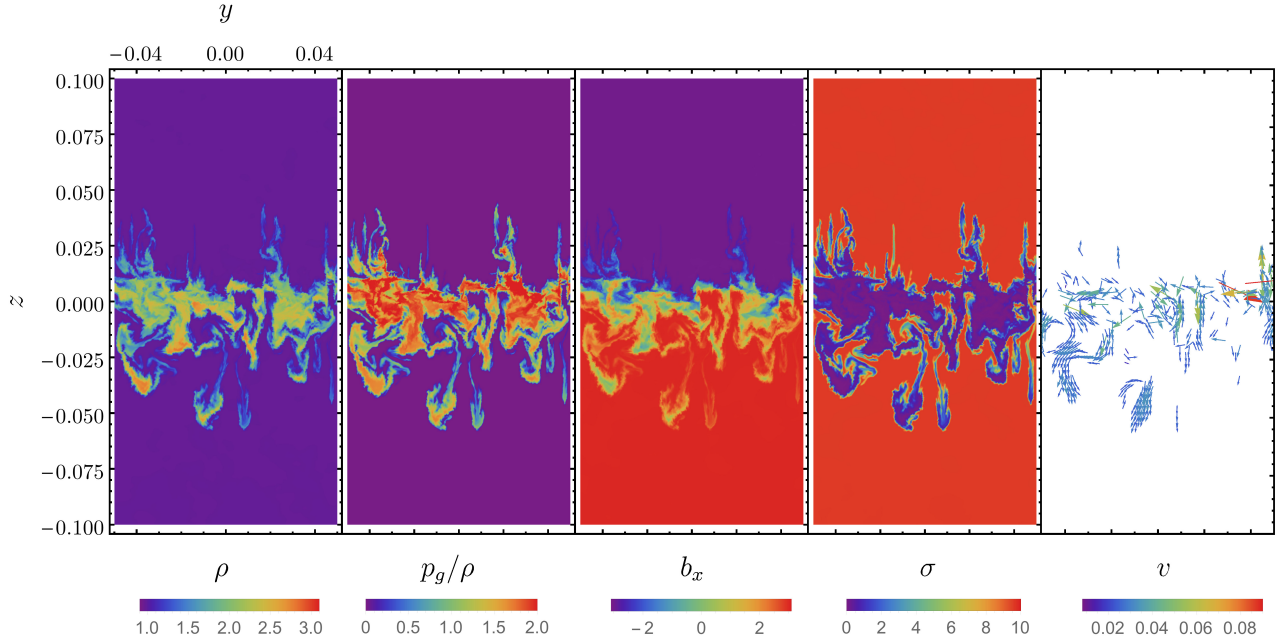


Figure 9. State of various quantities for the high mode number ($m_0 = 10$) perturbation with $g = 0.1$ at $t = 9$. Shown here are the gas density (ρ), ratio of gas pressure and density (p_g/ρ), the \hat{x} -component of the magnetic field (b_x), magnetization (σ), and gas velocity (\mathbf{v}).

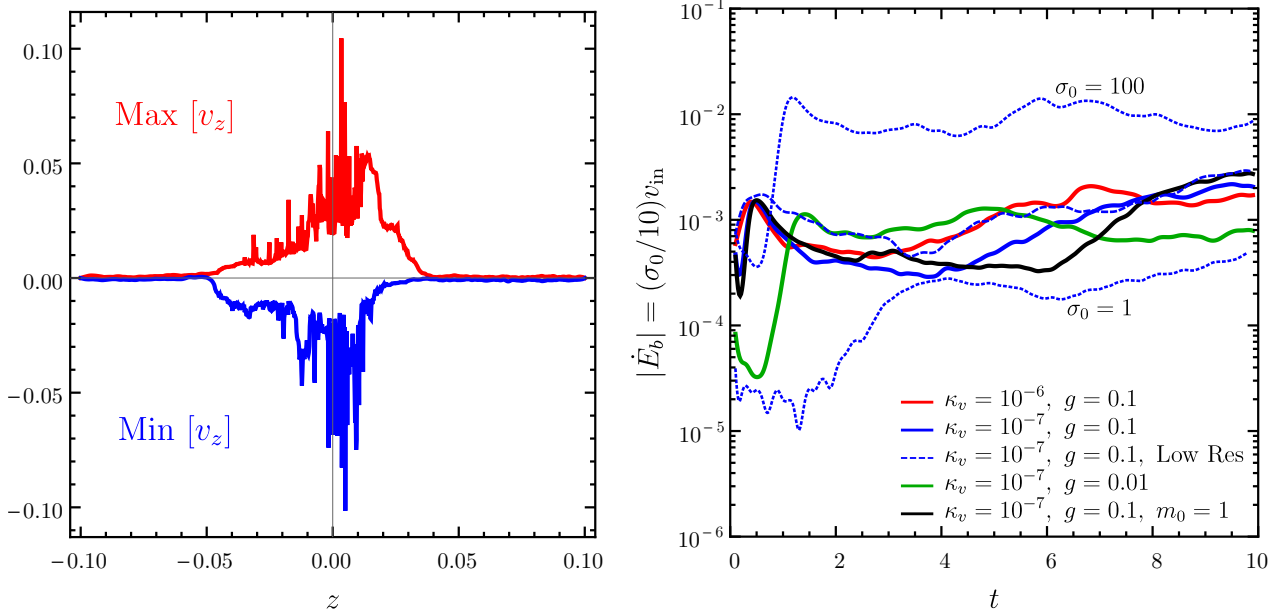


Figure 10. (Left) Peak velocity in the \hat{z} -direction at a given z -coordinate and across all y values, for the simulation shown in Fig. 9 with high mode number ($m_0 = 10$) perturbation and $g = 0.1$. In the highly mixed region, near the middle of the simulation box where the current layer was initialized, fluid velocities reach $|v_z| \sim 0.1$, where the initial velocity perturbation amplitude was $10^{-7} v_A$. The peak v_z shows no clear dependence on κ_v , g , or σ_0 . **(Right)** Magnetic energy dissipation rate due to reconnection in the simulated volume ($|\dot{E}_b| \approx L_y L_z b |\dot{b}|$) for $m_0 = 10$ perturbation. The result from a low-resolution [256 \times 512] simulation is also shown.

small wavelength ($m > 1$) modes at early times as can be seen in the mode spectrum shown in the right-panel of Fig. 4. At this stage, the spatially averaged mode amplitude $\langle f_m \rangle$ grows super-exponentially. (2) *Linear stage*: Very quickly (~ 20 light-crossing times of the width of the box), the instability enters the linear stage where the growth rate is determined by the dominant $m \sim m_0 = 1$ mode and

the magnitude of the effective gravitational acceleration; the power in modes much larger than m_0 is relatively small in this stage. Due to significant mixing of modes higher than m_0 , the resultant growth rate corresponds to a mode with $\lambda = 0.08 \lesssim \lambda_0 = 0.1$. The linear stage commences at the same time in all averaged regions of size Δz , which is expected since Δz is centered at the current layer. The

same behavior is seen for the time at which the instability enters the non-linear stage. In addition, since the growth rate of the instability in the linear regime only depends on the magnitude of the effective gravity and initial wavelength of the mode, it is not expected to vary with Δz . The growth rate curves shown in Fig. 4 show excellent agreement with this expectation. (3) *Sub-linear stage*: Eventually, the non-linear stage of the instability sets in and the growth rate of the instability slows down. This is marked by a plateau in the Fourier mode amplitude with time.

It is important to stress here that the “linear” stage – stage (2) above – that is used for comparison, actually corresponds to $\ln\langle f_m \rangle \propto \eta_{mt}$, i.e. a linear growth of the logarithm of the perturbation amplitude $\langle f_m \rangle$, and therefore to an exponential growth of $\langle f_m \rangle$ itself.

The growth rate of the instability scales as $\eta \propto g^{1/2}$, and therefore a higher effective gravity g should lead to a more evolved state at a given simulation time t . This can indeed be clearly seen in Fig. 5, which shows the evolution of the KSI for a higher effective gravity, $g = 0.1$ (e.g. by the deeper penetration of the density fingers below the hot current layer). Furthermore, the asymmetry between the upper and lower regions is now much clearer. It is interesting to note that the hot plasma dripping from the current layer does not simply move downwards in an approximately straight line, but instead starts to curl upwards. This effect is investigated in more detail in § 6 where we discuss the effects of buoyancy and secondary plasma instabilities on the dripping blobs.

In the left-panel of Fig. 6, we compare the growth rate of the mode amplitudes for the two cases with $g = \{0.01, 0.1\}$, where the higher effective gravity causes the instability to reach the linear stage earlier in time as compared to the lower g case. In the non-linear stage, a higher g causes the unmagnetized over-dense regions to *drip* faster into the lower cold magnetized region (Lyubarsky 2010b). This displacement of large volumes of the hot layer downwards is reciprocated by the upward movement of bulk plasma from the lower region. The meeting of the rising bulk plasma blobs with thinner regions of the hot layer leads to the launching of thin plumes upwards (like when a stone is thrown into water).

The dripping of the unmagnetized fluid brings the two magnetized fluids of the striped wind into contact that undergo resistive dissipation of the entrained magnetic field. This has the effect of destroying magnetic energy and consequently heating up the fluid. As a result, the thermal energy should increase due to increase in the amount of hot fluid. The temporal evolution of volume averaged magnetic energy density $\langle U_b \rangle$, thermal energy density $\langle U_{th} \rangle$, and Lorentz factor of fluid elements $\langle \gamma \rangle - 1$ is shown in the right panel of Fig. 6. Since the bulk motion of the fluid elements remains non-relativistic, most of the dissipated energy goes into the internal energy of the relativistic gas rather than the kinetic energy. Although the growth rate of the mode amplitude did not show any dependence on κ_v , the temporal evolution of the magnetic energy, and correspondingly the thermal pressure, indeed does. A larger κ_v yields a faster magnetic energy decay rate in the earlier part of the non-linear phase; the two rates are similar in the later part. The former result is also true for the case with higher effective gravity.

4.2 Wavelength Comparable to the Size of the Current Sheet ($k\Delta \approx 1$)

Higher mode number perturbations ($m_0 > 1$) with wavelength comparable to the size of the current layer are most interesting as they are expected to yield vigorous disruption of the current layer. To achieve that we introduce perturbations with mode number $m_0 = 10$

or equivalently with wavelength $\lambda_0 = \Delta = 0.01$. The development of the instability in this case for $g = 0.1$ is shown in Fig. 7. In comparison to the single-wavelength case, the instability clearly shows more structure, which simply reflects the smaller wavelength of the seed perturbation. In both cases, the density fingers eventually penetrate to approximately similar depths at similar simulation times. This is expected since the effective gravity is the same in both cases.

In the linear stage, the instability grows at the rate for a mode with $\lambda \sim \lambda_0$, as shown in the left-panel of Fig. 8, where excitation of various modes both with $m < m_0$ as well as $m > m_0$ can be seen in the right-panel. The mode spectrum is more complex in this case and lacks the clear suppression of power for modes away from m_0 , as was seen in the single wavelength case.

To glean further information regarding the dynamical evolution of the instability, in Fig. 9 we show the state of the thermal pressure to rest mass density ratio p_g/ρ , magnetic field orthogonal to the page b_x , magnetization σ , and the fluid velocity \mathbf{v} in the y - z plane, along with the density ρ for comparison. These quantities are shown at time $t = 9$ where their state serves as a proxy to the amount of mixing that has occurred between the magnetized and unmagnetized fluids as well as the two magnetized fluids with oppositely oriented magnetic field lines. The degree of mixing between the magnetized and unmagnetized fluids, as it appears in the plot showing σ , is a good indicator of the amount of magnetic diffusivity that artificially dissipates magnetic energy. On the other hand, the level of mixing between the two magnetized fluids, as can be seen most clearly in the plot showing b_x , is what determines the rate of magnetic energy dissipation. We stop the simulation before the density fingers reach the bottom of the simulation box to avoid the final solution from being affected by the boundary conditions. Since there is no large scale directed flow towards the hot layer, the mixing is purely determined by the action of the effective gravity. The unmagnetized hot fluid has to drip out before the two magnetized regions can come into contact and undergo magnetic reconnection.

5 RECONNECTION RATE

Most magnetic reconnection models feature an ordered bulk flow towards the current layer, in which case the velocity of this bulk flow, v_{in} , just upstream of the current layer provides a good measure of the reconnection rate. However, this is a good measure of the reconnection rate only if the flow towards the current layer is ordered on large scales. In the simulations shown in this work, we find that the fluid motions in the mixing region are highly turbulent and lack order on larger scales. In the left-panel of Fig. 10, we plot the peak velocity in the \hat{z} -direction, which is orthogonal to the direction of the equilibrium magnetic field, $\hat{z} \perp \mathbf{b}_0$. The peak velocity of $|v_z| \sim 0.1$ is reached near the middle of the simulation box where the current layer was initialized and where the two magnetized regions undergo the maximum amount of mixing and reconnection. Near the top and bottom of the simulation box, where no reconnection is expected, the fluid velocity remains much smaller. Furthermore, practically the same level of peak velocity is attained, regardless of κ_v , g , and σ_0 , in all the simulations that we performed. This suggests that $|v_z| \sim 0.1$ is the maximum attainable turbulent velocity. Nevertheless, it appears that in our physical setup $|v_z|$ does not serve as a good measure of the actual reconnection rate.

An alternative measure of the reconnection rate that works better in our case may be obtained by directly calculating from the simulation results the rate at which the magnetic field energy is

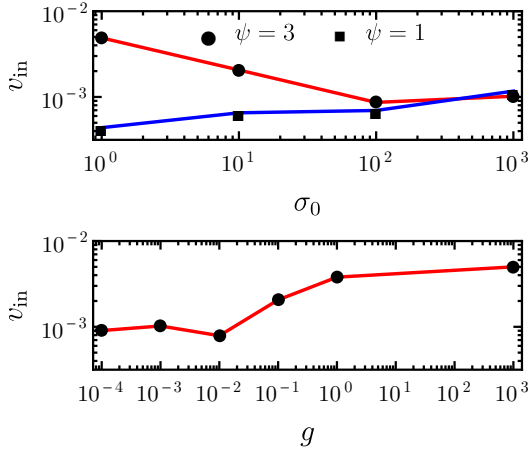


Figure 11. Reconnection rate as a function of the effective gravity g and fluid magnetization σ_0 . The rate of reconnection is defined using an effective upstream velocity v_{in} that is inferred from the rate of dissipation of magnetic field energy density. In the upper panel $g = 0.1$ and $\sigma_0 = 10$ in the lower panel; $\kappa_v = 10^{-7}$ for both panels. The dissipation rate for two values of the density ratio $\psi \equiv \rho_{h,0}/\rho_{c,0} = \{1, 3\}$ is shown as a function of σ_0 in the top-panel.

dissipated. The temporal evolution of the dissipated power,

$$-\dot{E}_b = -\frac{d}{dt} \int_{-L_z/2}^{L_z/2} dz \int_{-L_y/2}^{L_y/2} dy \frac{1}{2} b^2(y, z), \quad (19)$$

for both $m_0 = 1$ and $m_0 = 10$ cases is shown in the right-panel of Fig. 10, including results from a low-resolution (Low Res: 256×512) simulation. In all cases, there is a surge in the dissipation rate at very early times followed by saturation of the rate, which happens very quickly. The simulation is stopped at $t = 10$ at which point the density fingers almost reach the bottom of the simulation box. The magnetic field energy dissipation rate, after it has saturated, allows a straightforward determination of the reconnection rate,

$$|\dot{E}_b| = 2v_{\text{in}} L_y \frac{b_0^2}{2} = \sigma_0 \rho_{0,c} L_y v_{\text{in}}, \quad (20)$$

which yields $|\dot{E}_b| = v_{\text{in}}$ for $\sigma_0 = 10$, $\rho_{0,c} = 1$ and $L_y = 0.1$. We stress that here v_{in} represents the velocity of an ordered bulk inflow that would produce the same magnetic energy dissipation rate as the one that is produced in our simulations where the central mixing region is highly turbulent with no clear bulk flow. In this sense it serves as an effective bulk velocity, which is useful mainly for the purpose of comparison with the results of other magnetic reconnection models.

The dependence of v_{in} on σ_0 and g is shown in Fig. 11, which indicates that as σ_0 increases the efficiency of the reconnection process aided by the turbulent mixing declines. This can be understood as follows. The growth rate of the instability depends on the enthalpy density contrast between the hot and cold regions, such that $\eta \sim \sqrt{\Lambda g k}$ where $\Lambda = (w_{h,0} - w_{c,0}) / (w_{h,0} + w_{c,0})$, and $w_{h,0}$ and $w_{c,0}$ are respectively the initial enthalpy densities of the hot and cold regions. For $\rho_{h,0} = \psi \rho_{c,0} = \psi$ and the initial pressure $p_0 = b_0^2/2 = \sigma_0 \rho_{c,0}/2 = \sigma_0/2$, we find

$$\Lambda = \frac{1}{3} \left(1 + \frac{2(\psi - 2)}{1 + \psi + 3\sigma_0} \right) \xrightarrow{\sigma_0 \rightarrow \infty} \frac{1}{3}, \quad (21)$$

where $\Lambda < 1/3$ for $\psi < 2$, and $\Lambda > 1/3$ for $\psi > 2$. Therefore, when $\sigma_0 \sim$ a few the magnitude of ψ around the critical value of $\psi_c = 2$

causes the growth rate of perturbations to diverge, as shown in the top-panel of Fig. 11, which leads to a higher or lower v_{in} ; in the high- σ_0 limit v_{in} saturates regardless of the magnitude of ψ .

While in the high- σ_0 limit $v_{\text{in}} \rightarrow 10^{-3}$ for $g = 0.1$, increasing the effective gravity shows a promising increase in the reconnection rate. However, the maximum value of g in the simulation is limited by the dynamical time $t_{\text{dyn}} = g^{-1} = 10 - 100$ for $g = 10^{-1} - 10^{-2}$. This timescale should be longer than the free-fall time of a given fluid element where $t_{\text{ff}} = \sqrt{2\delta z/g} = \sqrt{2}$ for $g = 0.1$ and $\delta z = L_z/2 = 0.1$, the half length of the simulation box, i.e. one requires $t_{\text{ff}}/t_{\text{dyn}} = \sqrt{L_z/L_{\text{dyn}}} < 1$, which corresponds to $g < 1/L_z = 5$ for $L_z = 0.2$. The same result can be obtained from another consideration, that as g increases the length scale over which the total pressure is homogeneous also shrinks, which necessitates the need for a pressure gradient. The initial pressure was assumed to be uniform in all simulations since the vertical length of the simulation box $L_z \ll L_{\text{dyn}} = g^{-1}$.

The reconnection rate at $g \gg 1$ can only be probed at scales much smaller than used thus far in all the simulations. In order to do that, we ran additional simulations with a box size that was smaller by a factor of 10^{-3} for $g = 10^3$, $\sigma_0 = 10$, and $\kappa_v = 10^{-7}$. The resulting v_{in} is shown as the last point in the bottom-panel of Fig. 11 that clearly shows the saturation of the reconnection rate at $v_{\text{in}} \approx 5 \times 10^{-3}$; this rate is expected to be slightly lower for $\sigma_0 \gg 1$.

6 THE ROLE OF BUOYANCY, KELVIN-HELMHOLTZ INSTABILITY AND VORTICITY

The KSI causes unmagnetized blobs with higher enthalpy density to drip out of the hot plasma layer and sink into the lower enthalpy density magnetized cold plasma. These sinking blobs are subject to the RTI, which also gives rise to a *secondary* Kelvin-Helmholtz instability (KHI) that can grow over a few hundreds of light-crossing times (or sound crossing times) of the blob and shred it completely (see for e.g. Reynolds et al. 2005; Dong & Stone 2009, for discussion of buoyant blobs in galaxy clusters, where the bubbles are shredded after few sound-crossing times of the bubble). The blobs are also accelerated downwards more slowly because of the buoyancy force that acts in the direction opposite to gravity and has magnitude $\mathbf{F}_b \approx -w_c V_b \mathbf{g}$, where w_c is the enthalpy density of the ambient (cold) fluid and V_b is the volume displaced by the blob. This yields a reduced downward acceleration of the blob with magnitude $g_{\text{eff}} = (w_h - w_c)g/w_h \approx (w_{h,0} - w_{c,0})g/w_{h,0} = g/2$.

The effect of the buoyancy force and the KHI can be seen in Fig. 12 where we show the motion of a hot unmagnetized blob in a cold magnetized fluid. The hot blob, in pressure equilibrium with the cold magnetized fluid, is initialized with downward velocity $v_b = 0.01$ to mimic the downward dripping of hot plasma from the hot layer. Soon, the ram pressure exerted by the ambient fluid flattens the blob into a thin ribbon, the sides of which are curled upward due to the KHI. In the last snapshot of Fig. 12, we show the velocity vectors. The KHI gives rise to two symmetrical vortices which cause a drag force on the stretched-out blob that largely balances the downwards pull acting on it by the effective gravity, after correcting for the buoyancy force.

Interestingly, there is hardly any mixing between the blob and ambient fluid, which suggests that instabilities on the smallest scales at the interface between the blob and external fluid are suppressed. This behavior is contrary to what lower density blobs rising buoyantly in higher density inter-galaxy-cluster medium experience in numerical simulations. In the absence of any viscosity, the blobs are

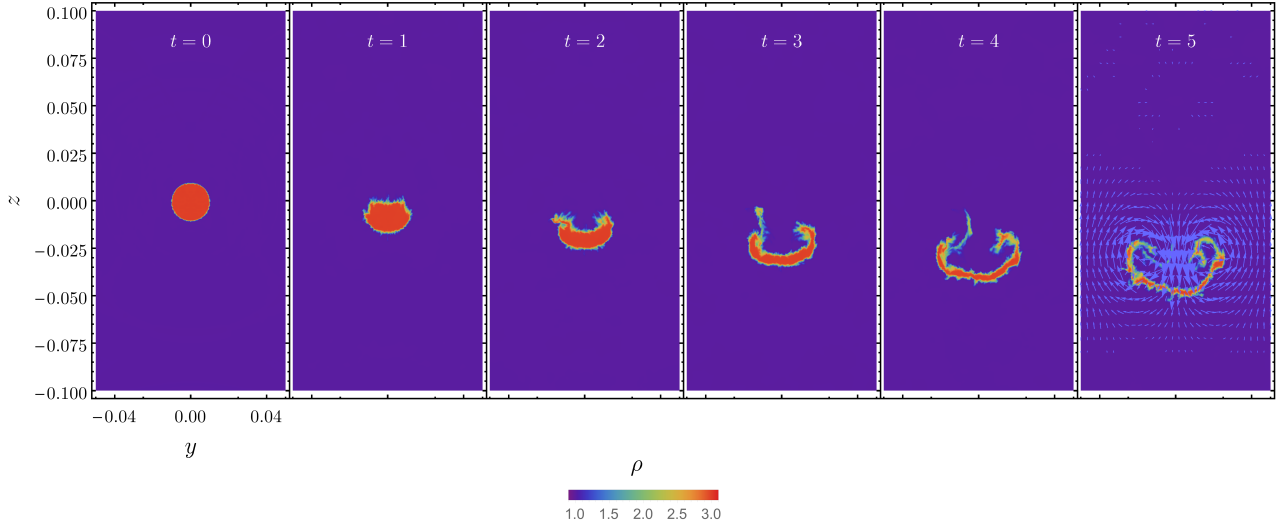


Figure 12. Density snapshots of an un-magnetized blob with initial downward velocity $v_b = 0.01$ in a magnetized fluid. The uniformly magnetized fluid, with magnetic field pointing out of the page, is cold and has magnetization $\sigma = 10$. Gravity points downward with $g = 0.1$. The blob is flattened due to the ram pressure of the ambient fluid. Onset of the Kelvin-Helmholtz instability leads to the development of symmetrical vortices as shown in the last snapshot, which provide an effective drag force that approximately balances the effective gravity accounting for the buoyancy force.

shredded and destroyed completely over few sound-crossing times. As shown by Reynolds et al. (2005); Dong & Stone (2009), viscosity stabilizes the secondary RTI and KHI and keeps the blob intact but still stretched out into a structure similar to what is shown in Fig. 12. The simulation shown in Fig. 12 does not have any artificial viscosity but only that due to numerical diffusion at the grid scale, which is small but enough to suppress small scale instabilities at the interface between the blob and ambient fluid.

The slower motion of the hot plasma due to such instabilities has a profound effect on the rate of reconnection. As argued earlier, reconnection in the scenario explored here depends critically on evacuation of hot plasma from the current layer. This allows the cold magnetized fluids with opposite polarity to come into contact and dissipate magnetic energy. If the dripping of plasma out of the hot layer slows down, then so will the rate of reconnection.

7 DISCUSSION

The ordered bulk inflow velocity v_{in} upstream of the current sheet is generally taken as a measure of the reconnection rate. In the steady-state Sweet-Parker reconnection, the inflow velocity is limited by the aspect ratio of the current sheet, such that $v_{in} = (\delta/L)v_A$, where δ and L are respectively the half width and half length (parallel to the upstream field direction) of the reconnection layer. Since in astrophysical plasmas usually $\delta/L \ll 1$, the Sweet-Parker reconnection cannot satisfy the fast energy dissipation rates needed in any bursting phenomena. Alternatively, 2D and 3D MHD simulations of relativistic reconnection have shown that $v_{in} \sim 0.1v_A$ (e.g. Watanabe & Yokoyama 2006), confirming the analytic result of Lyubarsky (2005).

It is important to note that these simulation are inherently different from the scenario explored here. In reconnection simulations similar to what is shown in Watanabe & Yokoyama (2006), plasma is forced out of the finite simulation box along the current layer due to the magnetic tension of the reconnected field lines. This allows the current layer to be evacuated at a much faster rate and yield high v_{in} . In addition, such simulations also invoke an explicit finite

resistivity, which greatly aids in enhancing the reconnection rate by setting up an X-type neutral point at the outset.

In this work we find turbulence rather than an ordered bulk flow in the reconnection region. Nonetheless, for comparison purposes we define v_{in} as the ordered bulk inflow velocity that would produce the same magnetic reconnection rate as we find in our simulations (see eq. (20)). With this definition we find that $10^{-3} \lesssim \beta_{in} \lesssim 5 \times 10^{-3}$, which is slower by up to two orders of magnitude. While β_{in} increases initially with increasing effective gravity, it quickly saturates at its final, but still low, value of $\beta_{in} \approx 5 \times 10^{-3}$ (for $\sigma_0 = 10$) due to the KHI, which produces vorticity and an effective drag force that inhibits fast evacuation of hot plasma from the current layer. We solve the equations of ideal MHD without any explicit resistivity. Therefore, magnetic field diffusion is minimal (only that due to numerical diffusion at the grid scale) which leads to most of the magnetic field away from the current layer to remain undisturbed. It is likely that the inclusion of finite resistivity could potentially significantly increase the reconnection rate.

Radiative cooling of particles in the current layer was neglected in this work, however, it can play an important role in determining the structure of the current layer and evolution of the KSI. If the scattering optical depth of the hot current layer is initially high then radiation will remain trapped inside it until photons can efficiently diffuse out of it. This particular scenario was explored analytically by Bégué, Pe'er, & Lyubarsky (2017), where they showed that in the optically thick case the pressure in the current layer is dominated by the radiation field, and the width of the layer remains larger by many orders of magnitude as compared to the optically thin case. In the latter case, since radiation can stream out, loss of pressure leads to compression of the current layer and therefore a large increase in gas density, which may in turn enhance the KSI. Interestingly, they showed that whether radiation streams out or remains trapped in the current layer has no effect on the dynamics of the outflow.

It was shown by Drenkhahn (2002); Lyubarsky (2010b); Bégué, Pe'er, & Lyubarsky (2017) that a Poynting flux dominated outflow with a striped wind structure will accelerate due to dissipation of energy via magnetic reconnection, such that

$d\Gamma/d\ln r \propto (\beta_{\text{in}} r)^{1/3}$ for $r < r_s$, where r_s is the saturation radius. The saturation radius $r_s \propto \Gamma_{\infty}^2/\beta_{\text{in}}$ is the point where most of the initial magnetic energy has already been tapped so that beyond it no further acceleration due to magnetic reconnection is possible and the flow simply coasts at a fixed Γ_{∞} . Therefore, a higher reconnection rate ($\beta_{\text{in}} > 0.1$) can yield a (up to an order of magnitude) lower saturation radius. As argued earlier, this can be facilitated by the existence of even a small resistivity in the flow.

In this work, we assumed an ideal scenario of completely anti-parallel magnetic field lines close to the current layer. In order to make this picture more realistic, allowance should be made for magnetic field shear between the two regions (1 and 3) with opposite polarity, such that there is a finite misalignment angle $\theta_{1,3}$ between the field lines. Understanding of the KSI in this case is important since magnetic field line tension of the misaligned field lines can stabilize the instability. This will be the subject of a future analytic work (Gill, Granot, & Lyubarsky, in preparation). Exploring such a scenario numerically necessarily requires 3D simulations, which are also left for a future study.

ACKNOWLEDGEMENTS

We would like to thank Omer Bromberg for numerous discussions on numerical MHD methods. RG, JG and YL acknowledge support from the Israeli Science Foundation under Grant No. 719/14. RG is supported by an Open University of Israel Research Fund. All simulations in this work were carried out on an Open University of Israel computer cluster.

REFERENCES

- Beckwith, K. & Stone, J. M. 2011, *ApJS*, 193, 6
 Begelman, M. C. 1998, *ApJ*, 493, 291
 Bégué, D., Pe'er, A. & Lyubarsky, Y. 2017, *MNRAS*, 467, 2594
 Blandford, R. D. & Payne, D. G. 1982, *MNRAS*, 199, 883
 Blandford, R. D. & Znajek, R. L. 1977, *MNRAS*, 179, 433
 Bromberg, O. & Tchekhovskoy, A. 2016, *MNRAS*, 456, 1739
 Coroniti, F. V. 1990, *ApJ*, 349, 538
 Dong, R. & Stone, J. M. 2009, *ApJ*, 704, 1309
 Drenkhahn, G. 2002, *A&A*, 387, 714
 Drenkhahn, G. & Spruit, H. C. 2002, *A&A*, 391, 1141
 Eichler, D. 1993, *ApJ*, 419, 111
 Fender, R. P., Belloni, T. M. & Gallo, E. 2004, *MNRAS*, 355, 1105
 Ghisellini G., 2011, in Paredes J. M., Ribo M., Aharonian F. A., Romero G. E., eds, High Energy Phenomena in Relativistic Outflows III meeting. Barcelona, June 2011. preprint (arXiv:1109.0015)
 Giannios, D. 2008, *A&A*, 480, 305
 Giannios, D., & Spruit, H. C. 2006, *A&A*, 450, 887
 Goedbloed, J., Keppens, R., & Poedts, S. 2010, *Advanced Magnetohydrodynamics: With Applications to Laboratory and Astrophysical Plasmas* (Cambridge: Cambridge Univ. Press)
 Granot, J. 2012, *MNRAS*, 421, 2442
 Granot, J. 2012, *MNRAS*, 421, 2467
 Granot, J., Komissarov, S. S. & Spitkovsky, A. 2011, *MNRAS*, 411, 1323
 Granot et al. 2015, *Space Sci. Rev.*, 191, 471
 Guo, F. et al. 2015, *ApJ*, 806, 167
 Heinz S., & Begelman M. C., 2000, *ApJ*, 535, 104
 Jun, B., Norman, M. L., & Stone, J. M. 1995, *ApJ*, 453, 332
 Kirk, J. G. & Skjæraasen, O. 2003, *ApJ*, 591, 366
 Komissarov S. S. 2012, *MNRAS*, 422, 326
 Komissarov S. S., Vlahakis N., Königl A., & Barkov M. V., 2009a, *MNRAS*, 394, 1182
 Komissarov S. S., Vlahakis N., & Königl A., 2010, *MNRAS*, 407, 17
 Krolik, J. H. & Piran, T. 2012, *ApJ*, 749, 92
 Kumar, P. Zhang, B. 2015, *Physics Reports*, 561, 1
 Landau, L. D. & Lifshitz, E. M. 1959, *Course of Theoretical Physics*, Oxford: Pergamon Press
 Levinson, A. 2010, *ApJ*, 720, 1490
 Lyatsky, W. & Goldstein, M. L. 2013, *Nonlin. Processes Geophys.*, 20, 365
 Lyubarsky, Y. 1992, *SvAL*, 18, 356L
 Lyubarsky, Y. 2005, *MNRAS*, 358, 113
 Lyubarsky, Y. E. 2009, *ApJ*, 698, 1570
 Lyubarsky, Y. E., 2010a, *MNRAS*, 402, 353
 Lyubarsky, Y. 2010, *ApJ*, 725, L234
 Lyubarsky, Y. & Kirk, J. G. 2001, *ApJ*, 547, 437
 Lyutikov, M. 2006, *New Journal of Physics*, 8, 119
 Lyutikov, M. 2011, *MNRAS*, 411, 422
 Lyutikov, M. & Blandford, R. 2003, [arXiv:astro-ph/0312347]
 Lyutikov, M. & Lazarian, A. 2013, *Space Sci. Rev.*, 178, 459
 McKinney, J. C. & Uzdensky, D. A. 2012, *MNRAS*, 419, 573
 Michel, F. C. 1971, *CoASP*, 3, 80
 Michel, F. C. 1994, *ApJ*, 431, 397
 Pétri, J. & Lyubarsky, Y. 2007, *A&A*, 473, 683
 Petschek, E. N. 1964, in *Proc. of an AAS-NASA Symp. on the Physics of Solar Flares*, ed. W. N. Hess (Washington, DC:NASA), 425
 Pudritz, R. E., Hardcastle, M. J., & Gabuzda, D. C. 2012, *SSRv*, 169, 27
 Reynolds, C. S. et al. 2005, *MNRAS*, 357, 242
 Ruderman, M. S., Terradas, J., & Ballester, J. L. 2014, *ApJ*, 785, 110
 Sironi, L. & Spitkovsky, A. 2011, *ApJ*, 741, 39
 Spruit, H. C., Foglizzo, T., & Stehle, R. 1997, *MNRAS*, 288, 333
 Spruit, H. C. 2010, in *Lecture Notes in Physics*, Vol. 794, ed. T. Belloni (Berlin: Springer), 233
 Stone, J. M. et al. 2008, *ApJS*, 178, 137
 Tchekhovskoy A., McKinney J. C., & Narayan R. 2008, *MNRAS*, 388, 551
 Tchekhovskoy A., McKinney J. C., & Narayan R. 2009, *ApJ*, 699, 1789
 Tchekhovskoy A., Narayan R., & McKinney J. C., 2010, *New Astron.*, 15, 749
 Terradas, J., Oliver, R., & Ballester, J. L. 2012, *A&A*, 541, A102
 Thompson, C. 1994, *MNRAS*, 270, 480
 Watanabe, N. & Yokoyama, T. 2006, *ApJ*, 647, L123
 Zhang, B. & Yan, H. 2011, *ApJ*, 726, 90

This paper has been typeset from a $\text{\TeX}/\text{\LaTeX}$ file prepared by the author.